SIAM J. SCI. COMPUT.
Vol. 48, No. 3, pp. A1260–A1283

EVALUATION OF RESONANCES: ADAPTIVITY AND AAA RATIONAL APPROXIMATION OF RANDOMLY SCALARIZED BOUNDARY INTEGRAL RESOLVENTS*

OSCAR P. BRUNO†, MANUEL SANTANA†, AND LLOYD N. TREFETHEN‡

Abstract. This paper introduces a novel algorithm that, employing rational approximants of randomly scalarized boundary integral resolvents, efficiently evaluates acoustic and electromagnetic resonances in both open and closed cavities. The desired cavity resonances (also known as "eigenvalues" for interior problems and "scattering poles" or "complex eigenvalues" for exterior and open-cavity problems) are obtained as the poles of associated rational approximants; both the approximants and their poles are produced by means of the recently introduced AAA rational approximation algorithm. In fact, the proposed resonance search method applies to any nonlinear eigenvalue problem associated with a given function $F : U \to \mathbb{C}^{d\times d}$, wherein, denoting $F(k) = F_k$, a complex value k is sought for which $F_k w = 0$ for some nonzero $w \in \mathbb{C}^d$. For the scattering problems considered in this paper, which include interior, exterior, and open-cavity problems, F_k is taken to equal a spectrally discretized version of a Green function–based boundary integral operator at spatial frequency k. In all cases, the scalarized resolvent is given by an expression of the form $u^* F_k^{-1} v$, where $u, v \in \mathbb{C}^d$ are fixed random vectors. The proposed adaptive search strategy relies on use of a rectangular subdivision of the resonance search domain which is locally refined to ensure that all resonances in the domain are captured. The approach works equally well in the case in which the search domain is a one-dimensional set, such as, e.g., an interval of the real line, in which case the rectangles used degenerate into subintervals of the search domain. A variety of numerical results are presented, including comparisons with well-known methods based on complex contour integration, and a discussion of the asymptotics that result as open cavities approach closed cavities—in all, demonstrating the accuracy provided by the method, for low- and high-frequency states alike.

Key words. eigenvalues, resonances, AAA rational approximation, integral equations, adaptive algorithm, high frequency

MSC codes. 65M38, 65M99, 47J10, 41A20

DOI. 10.1137/24M1690680

1. Introduction.

We are concerned with the problem of evaluation of resonances supported by open and closed cavities and other scattering structures, which are obtained as solution pairs (u, k) of the eigenvalue problem

$$\Delta u + k^2 u = 0 \tag{1}$$

with eigenfunction u and eigenvalue k^2, posed on an interior or exterior domain Ω, with homogeneous boundary conditions of, e.g., Dirichlet, Neumann, or other types on the boundary $\Gamma = \partial\Omega$. For definiteness, however, this paper restricts attention to eigenvalue problems subject to Dirichlet boundary conditions

$$u|_\Gamma = 0, \tag{2}$$

*Submitted to the journal's Numerical Algorithms for Scientific Computing section September 5, 2024; accepted for publication (in revised form) December 8, 2025; published electronically May 6, 2026.

https://doi.org/10.1137/24M1690680

Funding: The work of the first author was supported by NSF contract DMS-2109831 and by AFOSR contracts FA9550-21-1-0373 and FA9550-25-1-0015. The work of the second author was supported by National Science Foundation Graduate Research Fellowship grant 2139433.

†Computing and Mathematical Sciences, Caltech, Pasadena, CA 91125 USA (obruno@caltech.edu, msantana@caltech.edu).

‡School of Engineering and Applied Sciences, Harvard University, Cambridge, MA 02138 USA (trefethen@seas.harvard.edu).

where the domains Ω under consideration include both the interiors and exteriors of closed curves, as well as the complements of open curves. (Despite the focus of the current contribution on scattering problems, the method introduced here is general and, indeed, other nonlinear eigenvalue problems (NEPs) unrelated to boundary integral operators are considered in this paper as well.) Once approximated by discretized versions of the problem's boundary integral operators (which is done in this paper on the basis of the open- and closed-curve integral equation algorithms of [12, 18, 29]; see also [13]), the resonance-search problem is reduced to the solution of a related NEP for a certain function $F : U \to \mathbb{C}^{d\times d}$, wherein, denoting by $F(k) = F_k$ a relevant integral operator, a complex value k is sought for which

$$F_k w = 0 \quad \text{for some nonzero} \quad w \in \mathbb{C}^d. \tag{3}$$

As is well known [16], discretizing NEPs for differential operators can lead to various challenges, including spurious discrete poles and slow convergence of eigenvalues. However, as rigorously shown in a different yet related setting—and further discussed in Remark 2 below—boundary-integral methods for the Laplace eigenvalue problem considered here are not subject to such difficulties [38].

The proposed algorithm seeks the desired resonant values k, for which (3) holds, as poles of the randomly scalarized resolvent

$$S(k) = S(k; u, v) = u^* F_k^{-1} v, \quad \text{where} \quad u, v \in \mathbb{C}^d \quad \text{are fixed random vectors.} \tag{4}$$

This approach is justified in Appendix A, where it is shown that such poles coincide with those of F_k^{-1} with probability one—as illustrated numerically in section 6.2. The poles of $S(k)$, in turn, are obtained as poles of rational approximants of (4); both the rational approximants and their poles are produced numerically by means of the recently introduced AAA rational-approximation algorithm [34]. The proposed eigensolver additionally incorporates an adaptive search strategy and a secant method [40] termination stage. The adaptive search strategy relies on use of a rectangular subdivision of the resonance search domain which is locally refined to ensure that all resonances in the domain are captured. The adaptivity approach works equally well in the case in which the search domain is one-dimensional, such as, e.g., an interval of the real line, in which case the rectangles used degenerate into subintervals of the search domain. The secant method termination stage, in turn, is an important element in the proposed algorithm, which enables (i) exponentially fast convergence to near machine precision accuracy starting from AAA-based results of lower accuracy; (ii) reliable error estimation; and (iii) a capability to reliably screen the spurious eigenvalues that can (rarely) be produced by the AAA algorithm. In all, the overall proposed approach is simple, easy to implement, and rapidly convergent, and it requires limited computation besides the embarrassingly parallelizable evaluation of the scalarized resolvent at various wavenumbers k. A variety of numerical results presented in this paper demonstrate the character of the proposed approach: the method yields highly accurate approximations of scattering resonances and solutions of other NEPs, even in cases involving high frequencies.

A significant literature has developed in recent years in connection with the solution of NEPs. As discussed in the survey article [25], solution methods include root finding methods, contour integration methods, and methods based on linearization of F_k, all of which have been applied to the computation of resonances [3, 4, 21, 33, 38, 43]. (A discussion of certain advantages of the proposed approach over contour integration methods—particularly its notable flexibility regarding the required sampling of the

resolvent operator in the complex plane—is presented in section 6.4.) In turn, a set of methods for the NEP that, like the present paper, rely on use of AAA rational approximation have recently been developed [22, 24, 28], and specifically, the contributions [22, 24] apply the AAA algorithm to the scalarized resolvent (4). But in these contributions the AAA algorithm is applied in a manner different to the one we use: in those contexts a rational approximation is employed to produce a linearization of F_k whose eigenvalues approximate the desired eigenvalues, whereas the present paper directly uses the poles of the rational approximant of S as approximants of the desired eigenvalues. Closer to our work is the AAA-based algorithm introduced in [8, 10], which considers the transmission of plane waves by a periodic dielectric system. In that approach, numerical solutions of the transmission problem are obtained by means of the finite element method and from such solutions the rational approximant of the coefficient of transmission across the structure is produced—whose poles near the real axis are indicative of the resonant character of the structure, in that they incorporate information concerning some of the structure's complex eigenvalues.

In view of the strengths of the various algorithmic components it incorporates, the proposed algorithm is flexible, accurate, and efficient. The algorithm's use of rational approximations allows for utilization of scalarized resolvent data points on arbitrary sets of frequencies, enabling, in particular, the use of arbitrarily distributed data points on the boundaries of rectangles—which greatly facilitates the design of the adaptive strategy proposed in this paper. Further, use of simple intervals of the real line suffices for evaluation of real eigenvalues. The secant method termination stage, finally, provides significant benefits concerning accuracy and reliability, as mentioned in points (i)–(iii) above.

This paper is organized as follows. Sections 2 and 3 review the integral equation and associated numerical schemes used in this paper to represent solutions of the Helmholtz equation (1) for open and closed two-dimensional domains. Section 4 provides a brief description of the AAA algorithm. The overall proposed approach for the solution of NEPs is then described in section 5. A variety of numerical results presented in section 6 include NEPs unrelated to Laplace eigenvalues, comparisons with well-known methods based on complex contour integration, illustrations concerning low- and high-frequency Laplace eigenvalue problems for open and closed cavities, as well as the asymptotics that result as open cavities approach closed cavities—in all, demonstrating the accuracy provided by the method for low- and high-frequency states alike.

2. Eigenvalue problems, Green functions, and integral operators. We consider eigenvalue problems of the form (1), posed in open two-dimensional spatial domains Ω with smooth boundaries Γ, and with homogeneous boundary conditions on Γ. Three types of spatial domains are considered in this paper, namely, domains Ω equal to (a) the complement Γ^c of an open arc Γ in $\mathbb{R}^2$; (b) the region interior to a closed curve Γ in $\mathbb{R}^2$; and (c) the region exterior to a closed curve Γ in $\mathbb{R}^2$. For definiteness this paper mostly concerns eigenvalue problems under homogeneous Dirichlet boundary conditions (2) for each of these domain types. Homogeneous Neumann and Zaremba boundary conditions can be handled similarly [2, 3, 29]; in fact, results of Neumann problems produced by the proposed algorithm are briefly mentioned in section 6.5.

Our treatment of the problem (1)–(2) is based on use of the two-dimensional Helmholtz Green function $G_k(x,y) := \frac{\mathrm{i}}{4}H_0^1(k|x-y|)$ (where $k \neq 0$ and where H_0^1 denotes the Hankel function of the first kind of order 0) and the associated single-layer potential $\mathcal{S}_k : H^{-1/2}(\Gamma) \to H^1_{\mathrm{loc}}(\Omega)$ with surface density $\psi \in H^{-1/2}(\Gamma)$, given by

$$\mathcal{S}_k[\psi] = \mathcal{S}_k[\psi](x) := \int_\Gamma G_k(x,y)\psi(y)\,ds_y, \quad x \in \Omega, \quad \text{for closed curves } \Gamma. \tag{5}$$

The eigenfunction u may then be represented as

$$u(x) = \mathcal{S}_k[\psi](x), \quad x \in \Omega. \tag{6}$$

In view of the well-known continuity of the single-layer potential $\mathcal{S}_k = \mathcal{S}_k(x)$ as a function of $x \in \mathbb{R}^2$ up to and including the boundary Γ (see [17, 31]), scattering and eigenvalue problems involving both open and closed curves can be formulated in terms of the single-layer potential. However, as suggested in (5) and discussed in what follows, we employ this operator in its present form only for closed curves. Accordingly, we define the boundary integral operator $F_k : H^{-1/2}(\Gamma) \to H^{1/2}(\Gamma)$ by

$$F_k[\psi] = \int_\Gamma G_k(x,y)\psi(y), ds_y, \quad x \in \Gamma, \quad \text{for closed curves } \Gamma, \tag{7}$$

where $H^{\pm 1/2}(\Gamma)$ denote the standard Sobolev spaces; see [31].

Although the expression (7) may also be applied to open curves Γ—in which case the operator may be viewed as a map from the open-curve Sobolev space $\widetilde{H}^{-1/2}(\Gamma)$ into $H^{1/2}(\Gamma)$ (see [29]), a different formulation is adopted in this work for the open-curve case. Indeed, for open curves, it is both theoretically and computationally advantageous to employ a modified form of (7) that explicitly accounts for the edge singularities inherent in such geometries. As shown in [12, 29], the open-arc integral equation problem can be formulated within the framework of Sobolev spaces $H^s_{\mathrm{e}}(2\pi)$ for $s \in \mathbb{R}$. These spaces consist of 2π-periodic, even functions that admit cosine series expansions with coefficients decaying at a rate determined by the smoothness index s (see Appendix B). This alternative formulation addresses the edge singularities of the function ψ by explicitly factoring out a known singular term. To do this a smooth parametrization $r = r(t)$ of the open curve Γ, with $t \in [-1,1]$, is used, and the reformulated density is expressed as

$$\psi(r(t)) = \frac{\phi(r(t))}{\sqrt{1-t^2}}, \tag{8}$$

where ϕ is a smoother function, as detailed in Remark 1. By introducing a cosine change of integration variables, the square root term in the denominator is canceled by the corresponding Jacobian, and, thus, letting $\widetilde{\psi}(\theta) = \phi(r(\cos(\theta))$, the closely related integral expression

$$F_k[\widetilde{\psi}](\theta) = \int_0^\pi G_k(r(\cos(\theta)), r(\cos(\theta')))\widetilde{\psi}(\theta')\tau(\cos(\theta'))d\theta', \quad \theta \in \mathbb{R}, \quad \text{for open arcs } \Gamma, \tag{9}$$

is obtained, where $\tau(t) = |dr(t)/dt|$. As shown in [12, 29], for each $s \in \mathbb{R}$, (9) defines an operator

$$F_k : H^s_{\mathrm{e}}(2\pi) \to H^{s+1}_{\mathrm{e}}(2\pi) \tag{10}$$

which is invertible, bicontinuous, and compact. Using the same parameterization and cosine change of variables we also introduce the open-arc single-layer potential (5),

$$S_k[\widetilde{\psi}] = S_k[\widetilde{\psi}](x) = \int_0^\pi G_k(x, r(\cos(\theta')))\widetilde{\psi}(\theta')\tau(\cos(\theta'))d\theta', \quad x \in \Omega, \quad \text{for open arcs } \Gamma, \tag{11}$$

where $S_k[\widetilde{\psi}] : H^s_{\mathrm{e}}(2\pi) \to H^1_{\mathrm{loc}}(\Omega)$.

Remark 1. As mentioned above, the function ϕ resulting from the change of unknown (8) is smoother than the original unknown ψ. As an example, in view of (10), letting $\widetilde{\psi}$ denote either an eigenfunction of the infinite-dimensional NEP $F_k[\widetilde{\psi}] = 0$ (whose poles and eigenspaces do not depend on s on account of the Fredholm theory analysis outlined in Appendix B) or a solution to the equation $F_k[\widetilde{\psi}] = f$ with a smooth right-hand-side f (which in terms of the operator (9) becomes $F_k[\widetilde{\psi}] = f(r(\cos(\theta)))$), and taking into account the specialized version [1, Thm. 4.14] of the Sobolev lemma, the corresponding function $\widetilde{\psi}$ is smooth, 2π-periodic, and even, i.e., $\widetilde{\psi} \in C^{\infty}_{\mathrm{e}}(2\pi)$, provided the curve Γ is itself of class C^{∞}. Since $\phi(r(t)) = \widetilde{\psi}(\arccos(t))$ it follows that $\phi(r(t))$, which is given by a rapidly convergent Chebyshev expansion, is in $C^{\infty}[-1,1]$, and, thus, $\phi \in C^{\infty}(\Gamma)$; cf. [19].

Just as the k-dependent operator (7) is, as noted above, well-suited for evaluating eigenvalues and corresponding eigenfunctions in both the interior and exterior of closed curves, the corresponding operator (9) is well-suited for computing eigenpairs in domains that are complements of open arcs. The details are provided by the following theorem.

THEOREM 1. *Let $k_0 \in \mathbb{C}$. Then, for both interior and exterior problems (resp., for open-arc problems), the following two statements are equivalent:*

(i) *There exists a density $\psi \neq 0$ such that $F_{k_0}[\psi] = 0$ (resp., there exists a density $\widetilde{\psi} \neq 0$ such that $F_{k_0}[\widetilde{\psi}] = 0$).*

(ii) *The value $k = k_0$ is a pole of the resolvent operator F_k^{-1} as a function of k.*

Additionally, we have as follows:

(iii) *For interior and exterior (resp., open-arc problems), if k_0 is a pole of the resolvent operator F_k^{-1}, then $\Im k_0 \leq 0$ (resp., $\Im k_0 < 0$).*

(iv) *For exterior closed-curve (resp., open-arc) problems, the eigenvalues k^2 satisfying (1)–(2) together with a radiation condition at infinity (cf. [41, sect. 9, eq. 7.36, 7.47] and comment regarding equation 7.36) of the form (6) for some $\psi \in H^{-1/2}(\Gamma)$ (resp., for some $\psi \in \widetilde{H}^{-1/2}(\Gamma)$), equal the squares k_0^2 of the poles k_0 of the resolvent operator F_k^{-1} that lie in the lower half-plane $\Im k_0 < 0$. For the corresponding problem in the interior of a closed curve the eigenvalues k^2 satisfying problem (1)–(2) equal the squares k_0^2 of the poles k_0 of the resolvent operator F_k^{-1} that lie on the real axis $\Im k_0 = 0$.*

(v) *If k_0^2 is an eigenvalue of the eigenvalue problem (1)–(2) and the pair (k_0, ψ) with $\psi \neq 0$ (resp., $(k_0, \widetilde{\psi})$ with $\widetilde{\psi} \neq 0$) satisfies $F_{k_0}[\psi] = 0$ (resp., $F_{k_0}[\widetilde{\psi}] = 0$), then an eigenfunction u for the interior and exterior closed-curve eigenvalue problems (resp., the exterior open-arc eigenvalue problem) is given by the potential (5) with $k = k_0$: $u = \mathcal{S}_{k_0}[\psi]$ (resp., by the potential (11) with $k = k_0$: $u = \mathcal{S}_{k_0}[\widetilde{\psi}]$).*

Proof. A proof of Theorem 1 for the interior and exterior closed-curve problems can be found in [41, sect. 9.7]. A corresponding proof for the open-arc case is given in Appendix B. ∎

In particular, Theorem 1 tells us that the integral equation setting just described reduces the eigenvalue problem (1)–(2) for interior and exterior closed-curve and open-arc problems to an NEP for the operator F_k, with values of k restricted to the lower half-plane.

3. Numerical instantiation of the integral operator F_k. The numerical implementations utilized in this paper for the Green function–based integral operator

(7) are based on the discretization methods presented in [18, sect. 3.6] (resp., [12, sects. 3.2, 5.1]) for closed (resp., open) curves in the plane. For simplicity, our computational examples restrict attention to smooth curves Γ and boundary conditions of Dirichlet type, although related methods are available [2, 12, 18, 37] that enable corresponding treatments for nonsmooth boundaries [2, 18] as well as Neumann, Robin, and Zaremba boundary conditions [2, 12, 37].

For both open- and closed-curve problems the methods [12, 18] discretize the single-layer operator F_k on the basis of Nyström-type methodologies—utilizing a sequence of points along the curve Γ for both integration and enforcement of the equation. For closed curves Γ the discretization is produced as the image under the curve parametrization of a uniform grid in the parameter interval $[0, 2\pi]$; in the case of open curves the discretization results as the image of a Chebyshev mesh in the parameter interval $[-1, 1]$. For the open-arc and closed-curve cases, respectively, the unknown functions $\widetilde{\psi}$ and ψ are expressed in terms of Fourier-based expansions in the parameter intervals, and the methods are completed by exploiting explicit expressions for the integral of products of a logarithmic kernel and the Fourier basis functions. As illustrated in [12] and other contributions mentioned above, these methodologies can produce scattering solutions with accuracies near machine precision on the basis of relatively coarse discretizations, even for configurations involving high spatial frequencies.

In particular, these procedures produce highly accurate numerical approximations of the integral operator F_k in (6)—which we exploit in the context of this paper to produce accurate numerical evaluations of eigenvalues and eigenfunctions. Per the theoretical discussions in section 2 and Appendix A, the poles of a randomly scalarized version of this integral operator correspond to Laplace eigenvalues in the various cases considered (see also Remark 2 below). The proposed algorithm evaluates these poles as poles of associated AAA rational approximants, and the corresponding eigenfunctions are obtained via consideration of a Gaussian elimination–based desingularization procedure described in section 5. For added accuracy, the methods in that section include the application of the secant method after an initial evaluation of poles. In practice we have observed that accuracies near machine precision are obtained for both eigenvalues and eigenfunctions on the basis of the overall proposed methodology; a number of related illustrations are presented in section 6.

Remark 2. As mentioned in the introduction, the discretization of NEPs can give rise to various challenges, including spurious or missing eigenvalues, incorrect multiplicities, and slow convergence [16]. However, reference [38] shows that Galerkin-based discretizations of integral operators F_k of the type considered here possess the following desirable properties:

(i) Every eigenvalue of the continuous problem is approximated by a sequence of discrete eigenvalues computed using increasingly refined discretizations.
(ii) No spurious eigenvalues are introduced by the discretization.
(iii) The discrete eigenvalues converge to the exact ones with an error bounded by the Galerkin approximation error.
(iv) The multiplicities of discrete and continuous eigenvalues agree, provided the discretization is sufficiently fine.

Although these results have not, to our knowledge, been extended to the context of the spectral discretization methods used in this paper, we expect similar properties (i)–(iv) to hold. Indeed, the proofs in [38] could likely be extended to the spectral setting by analyzing the discrete spectral operators defined on the finite-dimensional

approximation spaces spanned by the Fourier basis functions used in this work. (A related convergence analysis for spectral discretizations of integral equation–based scattering solvers is presented in [11].) Moreover, our experiments have consistently supported the suggestion that the proposed methods are not affected by the aforementioned challenges. A rigorous justification of these observations, however, lies beyond the scope of the present work and is left for future investigation.

4. Rational approximants and the AAA algorithm. The AAA algorithm is a greedy procedure for the construction of a rational approximant to a given complex-valued function f on the basis of its values on an N-point set $Z_N \subset \mathbb{C}$ (full details can be found in [34]). Given the set $\{(z, f(z)) \mid z \in Z_N\}$, the algorithm proceeds by selecting a sequence of points $z_j \in Z_N$, starting with some point z_1, which in principle can be selected arbitrarily, but which the MATLAB implementation [20] takes as a $z \in Z_N$ for which the function value $f(z)$ is farthest from the mean of the set $\{f(z) \mid z \in Z_N\}$. The remaining points are then selected inductively. Once points $z_j \in Z_N$ $(1 \le j \le m)$ have been chosen, with corresponding function values $f_j \equiv f(z_j)$, for a suitably chosen vector $w^m = (w_1^m, \ldots, w_m^m)$ of complex weights w_j^m satisfying $\sum |w_j|^2 = 1$, the procedure to obtain z_{m+1} starts by constructing the barycentric-form rational function

$$r(z) = \frac{n^m(z)}{d^m(z)} = \sum_{j=1}^{m} \frac{w_j^m f_j}{z - z_j} \Big/ \sum_{j=1}^{m} \frac{w_j^m}{z - z_j}, \tag{12}$$

where, as suggested by the notation used, $n^m(z)$ and $d^m(z)$ denote the numerator and denominator in the right-hand expression in (12). The vector w^m is selected as follows: calling $A_m = \{(\widetilde{w}_1, \ldots, \widetilde{w}_m) \in \mathbb{C}^m \mid \sum |\widetilde{w}_j|^2 = 1\}$, w^m is defined as a minimizer of the least-squares problem

$$w^m = \operatorname*{arg\,min}_{\widetilde{w} \in A_m} \sum_{z \in Z_N^m} |f(z) d_{\widetilde{w}}(z) - n_{\widetilde{w}}(z)|^2,$$

where $Z_N^m = Z_N \setminus \{z_j \mid j = 1, \ldots, m\}$, $n_{\widetilde{w}}(z) = \sum_{j=1}^m \frac{\widetilde{w}_j f_j}{z - z_j}$, and $d_{\widetilde{w}}(z) = \sum_{j=1}^m \frac{\widetilde{w}_j}{z - z_j}$. Once the minimizer w^m has been computed, z_{m+1} is defined as a point $z \in Z_N^m$ for which $|f(z) - n^m(z)/d^m(z)|$ is maximum. Then, the set $Z_N^{m+1} = Z_N^m \cup \{z_{m+1}\}$ is defined, and the process is continued until the relation

$$\frac{|f(z) - n^m(z)/d^m(z)|}{\max\{f(z) \mid z \in Z_N\}} < \varepsilon_{\text{tol}} \quad \text{for all } z \in Z \tag{13}$$

is satisfied—which marks the successful termination of the algorithm. The last rational function (12) obtained as part of this process provides the desired rational approximant. Clearly, for given f, ε_{tol}, N, and Z_N the algorithm may or may not terminate successfully. Remark 3 outlines the conditions under which termination of the AAA algorithm and reliable approximation of the function f and its poles can be consistently expected. It also highlights the necessary adaptive implementations which, as discussed in Remark 4, have been found in practice to ensure the desired convergence.

Remark 3. Two important considerations concerning the practical use of the AAA algorithm involve the parameters ε_{tol} and N:

(i) The tolerance ε_{tol} should not be set below the numerical accuracy of the function evaluations f_j, as use of lower values often leads to spurious poles in the

rational approximant. In particular, in the near double-precision computations considered most often in this paper, the choice $\varepsilon_{\text{tol}} = 10^{-13}$ was always made.

(ii) In practice it has been found that the effectiveness of the AAA algorithm additionally depends on the use of a sufficiently large value of N. In the context of this paper the choice $N \geq 200$ has consistently been found adequate for convergence to the value $\varepsilon_{\text{tol}} = 10^{-13}$. However, convergence of the AAA algorithm does not guarantee that the resulting rational approximant captures all poles of f within the desired region of the complex plane, thereby motivating the adaptive algorithms developed in section 5.

5. Solution of NEPs. The discussion in sections 2 and 3 reduces the eigenvalue problem (1)–(2) to NEPs for the single-layer operators (7) and (9) (and the corresponding discrete approximate operators introduced in section 3), with values of k restricted to the lower half-plane. This section presents numerical algorithms for the solution of these NEPs and, indeed, of general NEPs for which the resolvent operator $(F_k)^{-1}$ is a meromorphic function of k—for which the poles coincide with the eigenvalues of F_k. In view of Theorem 2 in Appendix A, and as indicated in section 1, the corresponding search for poles of the operator $(F_k)^{-1}$ is reduced, with probability one, to the search of poles of the scalarized resolvent $S(k)$ introduced in equation (4).

The proposed NEP algorithm thus obtains the eigenvalues k as the poles of a AAA rational approximant associated with the randomly scalarized resolvent $S(k)$. While, in principle, values of the scalarized resolvent $S(k)$ on any given subset of the complex plane may be used to obtain eigenvalues, throughout this paper we restrict attention to algorithms based on use of values $S(k)$ for k on a given curve $\mathcal{C}$ in the complex plane. Both open and closed curves $\mathcal{C}$ may be used, such as, e.g., the closed curves equal to the boundaries of either a rectangle or a circle, or the open curve equal to an interval $[a, b]$ contained in the real axis. Proceeding on the basis of such data, Algorithms 1 and 2 below seek to evaluate either eigenvalues contained on the union $\widetilde{\mathcal{C}}$ of $\mathcal{C}$ and its interior, if $\mathcal{C}$ is a closed curve, or eigenvalues along the curve $\mathcal{C}$, if $\mathcal{C}$ is an open curve. As noted in point (ii) of Remark 3, Algorithm 1 generically fails to capture all poles within the target region, $\widetilde{\mathcal{C}}$ or $\mathcal{C}$. Algorithm 2 addresses this limitation by incorporating a suitable adaptive strategy.

In detail, the pseudocode Algorithm 1 proceeds by first evaluating the scalarized resolvent $S = S(k)$ at a suitably selected set $Z_N = \{k_1, \ldots, k_N\}$ of points along $\mathcal{C}$ to obtain the set $G_N = \{(k_j, s_j) \mid s_j = S(k_j),\ j = 1, \ldots, N\}$. Using this set of pairs Algorithm 1 then obtains a rational approximant $r = r(k)$ by means of the AAA

Algorithm 1. Basic algorithm.

```
Select a set Z_N = {k_1, ..., k_N} which is a subset of an open curve C or a
  closed curve and its interior C̃
Choose random vectors u, v ∈ C^d
for j = 1, ..., N do
  | S(k_j) = u* F(k_j)^{-1} v
end
Compute a rational approximant r(z) associated with the set
  {(k_j, s_j) | s_j = S(k_j), j = 1, ..., N} using the AAA algorithm
Return the poles of r(z) in C or C̃
```

Algorithm 2. Adaptive algorithm.

Input: A set $\mathbf{C}$ which is either a rectangular region $\widetilde{\mathcal{C}}$ or real interval $\mathcal{C}$ and eigenvalues k from Algorithm 1 applied to $\mathbf{C}$

```
Function eigadaptive(k, C)
    Partition C dyadically in each dimension into sets C_i, which are
     rectangular regions if C is rectangular region or real intervals if C is a
     real interval.
    for each C_i do
        Compute n_i, the number of eigenvalues k in C_i
        Compute eigenvalues k̃ from Algorithm 1 applied to C_i
        Compute ñ_i, the number of eigenvalues k̃ in C_i
        if n_i = ñ_i then
            return k̃
        else
            return eigadaptive(k̃, C_i)
    end
```

algorithm, and, for a closed curve $\mathcal{C}$, the poles of $r(k)$ contained in $\widetilde{\mathcal{C}}$ (resp., for an open curve $\mathcal{C}$, the poles on $\mathcal{C}$ or, more precisely, at a distance $\leq \delta$ from C for a user-selected tolerance δ) are returned as approximations of eigenvalues of F_k.

Typically, Algorithm 1 finds all of the eigenvalues within $\mathcal{C}$ or $\widetilde{\mathcal{C}}$, as relevant, provided the number of such eigenvalues is not too large—say, in the range of 30 to 40 eigenvalues. This observation suggests the development of an adaptive version of Algorithm 1, which, as detailed in the pseudocode titled Algorithm 2, is specialized to searches for eigenvalues within either (i) a rectangular region $\widetilde{\mathcal{C}}$, or (ii) a real interval $\mathcal{C} = [a, b]$. The algorithm begins by applying Algorithm 1 to $\widetilde{\mathcal{C}}$ (resp., $\mathcal{C}$) using N points. This yields an initial approximation of the eigenvalues inside $\widetilde{\mathcal{C}}$ (resp., on $\mathcal{C}$), based on the poles of the computed approximant $r(z)$. Next, $\widetilde{\mathcal{C}}$ (resp., $\mathcal{C}$) is recursively subdivided dyadically along each dimension into smaller sets C_i, $1 \leq i \leq 4$ (resp., $1 \leq i \leq 2$). Algorithm 1 is then applied to each C_i, again using N points along each curve. The recursion terminates when the number of eigenvalues detected within a set C_i remains unchanged upon further subdivision. Clearly, the fact that Algorithm 1 is applicable to arbitrary curves and, in particular, to rectangular regions greatly facilitates the adaptive subdivision strategy used in Algorithm 2.

Remark 4. The AAA algorithm may fail to accurately produce the eigenvalues (either within a region $\mathcal{C} \subset \mathbb{C}$, or upon an interval $\mathcal{C} \subset \mathbb{R}$) if the set G_N does not adequately represent $S(k)$ along the curve $\mathcal{C}$. With reference to Remark 3(ii), in practice we have found that, for AAA tolerance $\varepsilon_{\text{tol}} = 10^{-13}$, the adaptive Algorithm 2 with $N \geq 200$ consistently produces all complex (resp., real) eigenvalues in the closed region $\widetilde{\mathcal{C}}$ (resp., on the interval $\mathcal{C}$).

Practice has shown that, provided the curve $\mathcal{C}$ encloses a sufficiently small number of eigenvalues, once convergence to a fixed set of poles has occurred, the poles obtained within $\mathcal{C}$ or $\widetilde{\mathcal{C}}$ correspond in a one-to-one fashion to all the eigenvalues in that region. Starting from such poles, eigenvalues with near machine precision accuracy can be obtained by means of one of two possible methods, namely (i) use of a subsequent "localized" AAA approximation applied to a few points around each eigenvalue obtained from Algorithm 2, or (ii) application of the secant method iteration

$$k_n = k_{n-1} - T(k_{n-1})\frac{k_{n-1} - k_{n-2}}{T(k_{n-1}) - T(k_{n-2})} \tag{14}$$

to $T(k) = 1/S(k) = 1/(u^* F_k^{-1} v)$, starting at each one of the eigenvalues obtained in the initial application of Algorithm 2. In regard to method (i), we have observed that use of localized AAA approximations over a circle of radius $\rho_{\text{conv}} = 10^{-5}$ works well in many cases, but generally tuning of the parameter ρ_{conv} is necessary for convergence and, indeed, it is difficult in practice to determine whether convergence to a given tolerance has occurred, except in test cases for which the eigenvalues are known beforehand. Fortunately, method (ii) does not present these difficulties: it results in convergence to the eigenvalue without use of tuning parameters, and the convergence history provides an error estimate for the eigenvalue produced. We therefore recommend this approach as the termination stage for each eigenvalue found by Algorithm 2, and we use it for all of the numerical examples presented in section 6. A comparison of these two termination stage algorithms is presented in the upper-right panel of Figure 4.

Eigenvectors corresponding to each eigenvalue can finally be obtained via evaluation, based on Gaussian elimination, of the nullspace of the matrix F_k at each eigenvalue k obtained. In detail, using Gaussian elimination with pivoting leads to an LU decomposition of the form $PF_k = LU$, where P is a permutation matrix, and where L and U are lower- and upper-triangular matrices, respectively. Using this decomposition the nullspace of F_k can be computed by a simple two-step procedure consisting of (a) selection of a set of canonical-basis vectors that are mapped to zero by the rows in the matrix U that are associated with the nonzero pivots, and (b) for each zero pivot in the matrix U, construction and solution of the reduced systems that result from the elimination of the rows and columns in U containing the zero pivots, and with right-hand sides equal to the negatives of each of the eliminated columns but excluding the column element in the eliminated row. Null vectors could also be computed by means of the singular value decomposition for sufficiently small problems such as the two-dimensional examples considered in this paper, but the singular value decomposition method would be problematic for larger problems such as those arising from scattering in three dimensions, whereas, in view of [36], GMRES-based iterative methods related to the LU-based approach mentioned above can be envisioned. An alternative considered in [8, sect. 2.2] produces eigenvectors on the basis of the rational approximation itself, albeit, according to our experiments, at the expense of some loss of accuracy. In this contribution the aforementioned Gaussian elimination procedure is used, as it requires no additional approximation after application of the secant-based refinement method, and as it results in accuracies comparable to those enjoyed by the eigenvalues themselves.

6. Numerical examples. Numerical illustrations of the proposed methodology are presented in what follows, including a demonstration of the performance of Algorithm 2 on NEPs unrelated to Laplace eigenvalues (section 6.1); an illustration of the almost-sure pole detection capability of the scalarized resolvent $S(k)$ (section 6.2); a set of examples concerning low-frequency Laplace eigenvalues (section 6.3); a comparison to complex contour integration methods (section 6.4); an exploration of the rate at which scattering poles associated with open arcs converge to the corresponding interior eigenvalues as the opening closes (section 6.5); and, finally, a set of examples concerning high-frequency Laplace eigenvalues and eigenfunctions (section 6.6). In all cases the eigenfunction images display the absolute value of the complex eigenfunction. All of the numerical illustrations presented in this paper utilize the AAA implementa-

tion included with Chebfun [20]. The code used to perform the numerical experiments is publicly available at https://github.com/manuelarturosantana/ScalResNEP

6.1. Adaptivity and exhaustive eigenvalue evaluation. This section illustrates the ability of Algorithm 2 to exhaustively evaluate the set of eigenvalues of a given NEP that are contained in a given region in the complex plane (see also the examples mentioned in the first paragraph of section 6.6). To do this, two well-known problems included in the NLEVP collection [7] are considered, namely, the "CD player problem" and the "Butterfly problem"; the corresponding eigenvalues are purely real in the first case and complex but not real in the second case. The CD player problem is an eigenvalue problem for a 60×60 matrix polynomial of the form $F(k) = k^2 I + kA_1 + A_0$ arising in the study of a CD player control task [15]. We restrict attention to the interval $[-50, 5]$ on the real axis, within which the problem has 60 eigenvalues with absolute values as small as $2.23e-4$ and as large as 41.1399; the real-interval version of Algorithm 2 was used with a total number of 300 points k_j along each subinterval. The second problem is the butterfly problem, in which eigenvalues of a 64×64 matrix polynomial $F(k) = \sum_{i=0}^{4} k^i A_i$ are sought. The matrices A_i are Kronecker products of linear combinations of the identity and nilpotent Jordan blocks [32]. We tackle the butterfly problem by employing Algorithm 2 applied initially to the box of side length 4 centered at the origin. This problem has 256 eigenvalues, and 100 values of k were used on each side of the square. Figure 1 displays the results produced by the proposed algorithm: in each case the proposed adaptive algorithm obtains all of the eigenvalues in the prescribed regions of the complex plane.

6.2. Illustration of the almost-sure pole detection via the scalarized resolvent $S(k)$. As indicated in the introduction and rigorously established by Theorem 2 in Appendix A, the poles of the scalarized resolvent coincide, with probability one, with the poles of the full resolvent operator. In other words, with probability one,

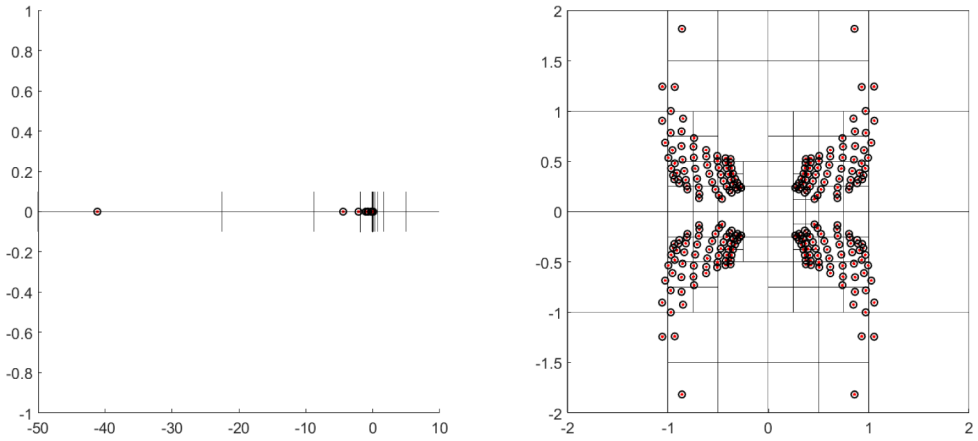

FIG. 1. *Demonstration of Algorithm* 2 *on two problems from the NLEVP set* [7]. *In both panels red points represent exact eigenvalues and black circles represent eigenvalues produced by the proposed numerical method. Black lines represent divisions related to the adaptive version of the algorithm. Left panel: The CD player problem, for which all* 60 *eigenvalues in the interval* $[-50, 5]$ *were found to at least* 7 *digits. Right: The butterfly problem, for which all* 256 *eigenvalues were found to at least* 10 *digits. For both problems, accuracy near machine precision subsequently resulted by applying the secant termination stage. The AAA-based termination method results in similar accuracy, but per points* (i) *and* (ii) *in section* 5 *the secant-based termination method is recommended.*

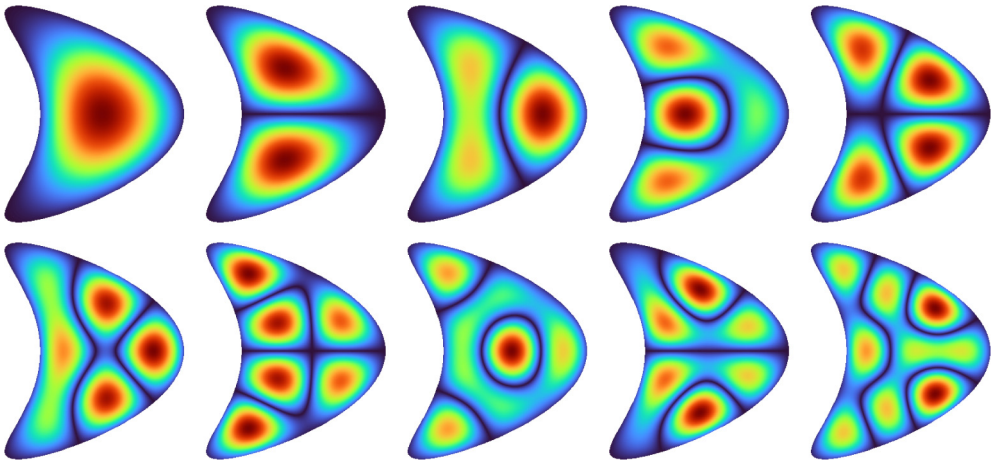

FIG. 2. *Low-frequency interior eigenvalue problems mentioned in section* 6.3*: the first* 10 *interior eigenfunctions for the kite-shaped domain. The associated frequencies* k *are listed in the left column of Table* 1.

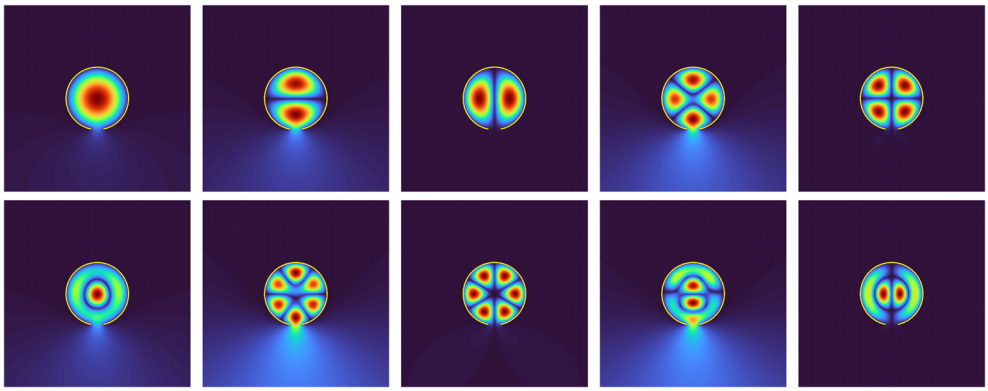

FIG. 3. *Low-frequency open-arc eigenfunctions, discussed in section* 6.3*, corresponding to the first* 10 *scattering poles of the open circle with imaginary parts less than* $-0.2i$*. The eigenfunctions are ordered left-to-right and top-to-bottom by increasing real part of the frequency. The associated frequencies* k *are displayed in the right column of Table* 1.

the selection of random vectors inherent in the definition of the scalarized resolvent $S(k)$ does not affect the poles of the scalarized resolvent. To illustrate this, Algorithm 2, including the secant method termination stage, was applied to the butterfly problem 1000 times, using 1000 different scalarized resolvent functions (4)—obtained from 1000 different pairs of uniformly distributed random vectors. The parameter values mentioned in section 6.1 were used in all cases. In all 1000 runs, Algorithm 2 produced all 256 butterfly eigenvalues, each with an error no greater than $8.8 \cdot 10^{-14}$.

6.3. Low-frequency eigenvalues. This section illustrates the character of the proposed eigensolver in the context of NEPs (3) associated with low-frequency Laplace eigenproblems (1) with boundary conditions (2). Thus, Figures 2 and 3 and Table 1 present Laplace eigenfunctions and eigenvalues for two structures, namely, a (closed) kite-shaped domain and a circular cavity with an aperture of $\pi/8$ radians. For the interior kite problem the eigenvalues are real, and they are thus obtained by means

TABLE 1

Using the specified values of ε_{tol} and η, the first and third tables present computed frequencies k, where k^2 is the computed eigenvalue of the eigenvalue problem (1)*; the corresponding eigenfunctions are displayed in Figures* 2 *and* 3*, with increasingly higher-frequency eigenfunctions arranged from left to right and top to bottom. All digits reported in the first and third tables are believed to be correct on the basis of a numerical convergence analysis. In contrast, the second table shows results from a low-accuracy computation of the kite eigenvalue problem; the underlined digits in that table match the corresponding digits in the high-accuracy eigenvalues presented in the first table.*

Kite	Kite	Open circle
$\varepsilon_{\text{tol}} = 10^{-13},\ \eta = \mathcal{O}(10^{-13})$	$\varepsilon_{\text{tol}} = 10^{-1},\ \eta = \mathcal{O}(10^{-1})$	$\varepsilon_{\text{tol}} = 10^{-13},\ \eta = \mathcal{O}(10^{-13})$
2.209856180349	2.209856160580 − 0.000000000000i	2.391850921204 − 0.000866833533i
3.215653682128	3.215649339554 − 0.000000000206i	3.785851440218 − 0.007551333804i
3.528868275787	3.528836817154 − 0.000000005950i	3.831519839558 − 0.000000810935i
4.303831479675	4.303687601771 − 0.000000319565i	5.066410135738 − 0.022753855105i
4.371112240590	4.370395770720 − 0.000001971373i	5.134599571714 − 0.000011845979i
4.906513621606	4.903841748469 − 0.000022407289i	5.486798760828 − 0.010839713761i
5.291183742145	5.288051279854 − 0.000052199257i	6.297659940294 − 0.044691641691i
5.461743432329	5.458708983780 − 0.000056893175i	6.377232306043 − 0.000071959651i
5.736410337307	5.723783304240 − 0.000354630699i	6.923647500434 − 0.056416692369i
6.172352448525	6.144174825865 − 0.001681646048i	7.015195622517 − 0.000013514954i

of Algorithm 2 with $\mathcal{C}$ equal to an interval in the real axis. In the open circle case the eigenvalues lie near the real axis; they were obtained using once again Algorithm 2, but this time using a rectangular curve $\mathcal{C}$ enclosing a finite section of the strip between the real axis and the horizontal line $\Im k = -0.2$; for such a thin strip the localization step was applied by iteratively subdividing the domain along the real axis only.

In order to estimate the error in the computed eigenvalues, the error in the discretization of the boundary integral operators, denoted by η, was estimated by means of a numerical convergence study for the solution of the equation

$$F_k[\psi](x) = e^{\mathrm{i}kp\cdot x} \quad x \in \Gamma \quad \text{with} \quad p = (1,0), \tag{15}$$

and $k = 6$. On the basis of these studies a discretization size was chosen so that $\eta = \mathcal{O}(10^{-13})$, leading to a corresponding error on the order of $\mathcal{O}(10^{-13})$ for all eigenvalues k. For eigenvectors v computed by the LU method discussed in section 5 the residual $\|F_k v\|$ (where $\|\cdot\|$ denotes the Euclidean 2 norm) was also on the order of $\mathcal{O}(10^{-13})$ resulting in similar accuracy for the eigenfunctions. Additionally, Table 1 displays the eigenvalues for the kite obtained using a coarser discretization of the boundary integral operators with $\eta = \mathcal{O}(10^{-1})$ and, in accordance with Remark 3(i), the tolerance ε_{tol} in the AAA algorithm set to $\varepsilon_{\text{tol}} = 10^{-1}$. Note that the same discretization was used for computation of all eigenvalues, and the error $\eta = O(10^{-1})$ in the discretization of the boundary integral operators resulted from a convergence study for the solution of (15) with $k = 6$; a corresponding error $\mathcal{O}(10^{-4})$ resulted for the solution of (15) with $k = 2$. (The trend of increased accuracy at lower frequencies observed in Table 1 reflects the correspondingly higher accuracy of the integral equation solutions obtained at lower frequencies by the discretization used, as well as the effectiveness of the secant method stage.)

6.4. Comparison with Integral Algorithm 1 in [9] and the block SS method [5]. It is most relevant in the context of this paper to compare the proposed algorithm to other eigensolvers which, like ours, are based on use of Green function representations. Most often such algorithms rely additionally on complex contour integration strategies for evaluation of eigenvalues [6, 14, 27, 30, 33, 35, 38, 42, 44], and

we therefore select for our comparison the two best-known and prototypical complex contour eigensolvers, namely, the block SS method [5] and Integral Algorithm 1 in [9]. To avoid potential confusion with Algorithm 1 presented in section 5 above, in what follows we refer to Integral Algorithm 1 in [9] as Beyn 1; for our comparisons we use the implementations of the Beyn 1 and block SS algorithms provided in [25].

The block SS method relies on use of matrices containing L columns of random vectors by computing the product

$$U^* F_k^{-1} V \in \mathbb{C}^{L\times L}, \quad \text{where} \quad U, V \in \mathbb{C}^{d\times L} \tag{16}$$

are matrices containing L random vectors as columns.

Additionally, per prescriptions in [5], a number $2P$ of associated moments of the k-dependent $L \times L$ matrix in (16) are computed and used to construct a generalized eigenvalue problem whose solution provides numerical values of the desired eigenvalues and eigenvectors. Here we determine the number $2P$ of moments used (which according to [25] should be such that PL is not smaller than the number of eigenvalues contained in the contour, counting multiplicities) on the basis of the SVD-based rank test introduced in [9]. For simple eigenvalues, such as appear most often for exterior scattering eigenvalues problems [26], it suffices [5] to choose $L = 1$ in the block SS method. Note that with this selection of the parameter L, the block SS algorithm is based on use of the scalarized resolvent (4)—exactly the same data utilized by Algorithm 1. The Beyn 1 method, in turn, utilizes the product in (16) with the matrix U^* replaced by the d-dimensional identity matrix. The number L of columns used in the Beyn 1 approach is selected on the basis of the aforementioned SVD-based rank test; in particular, the value L must at least equal the number of eigenvalues within the contour (counting multiplicities), and, to yield highly accurate results, it may need to be increased by a small number, perhaps as small as one or two (in accordance with the rank test), to account for the number of eigenvalues outside the contour but sufficiently close to it.

For our comparisons we consider the problem of evaluation of eigenvalues of the Dirichlet problem in the exterior of the kite-shaped curve used for the experiments in Figure 2. In detail, using Algorithm 1 as well as the block SS and Beyn 1 methods we evaluate the eigenvalues contained within the circular contour $\mathcal{C}$ with center at $3 - 1.5\mathrm{i}$ and radius 1, on the basis of equally spaced points along $\mathcal{C}$. The left panel in Figure 4 shows the eigenvalues within the curve $\mathcal{C}$ as computed by each method, while the corresponding right panel displays the error resulting from use of the various algorithms in the evaluation of the eigenvalue near $2.299 - 1.597\mathrm{i}$ as a function of the number of points used along the contour $\mathcal{C}$, using the computation by Algorithm 1 with secant method as the reference solution. Errors resulting from use of the two different accuracy refinement methods introduced in section 5, namely, the secant method and the localized AAA approximation, are included in the figure as well. The computed eigenvalues are presented in Table 2.

Figure 4 shows that Algorithm 1 and the block SS method converge at similar rates, at least for a range of frequencies. While Beyn 1 converges faster than Algorithm 1 and block SS without local refinement, use of a local refinement technique on any of the three methods leads to similar convergence rates for the eigenvalues. Moreover, in situations where computing the discrete system matrix and/or its LU factorization is undesirable or impractical—such as in large surface or volumetric discretizations in three-dimensional space envisioned in future work—Algorithm 1 may offer a significant advantage over Beyn 1. Indeed, the need for Beyn 1 to incorporate

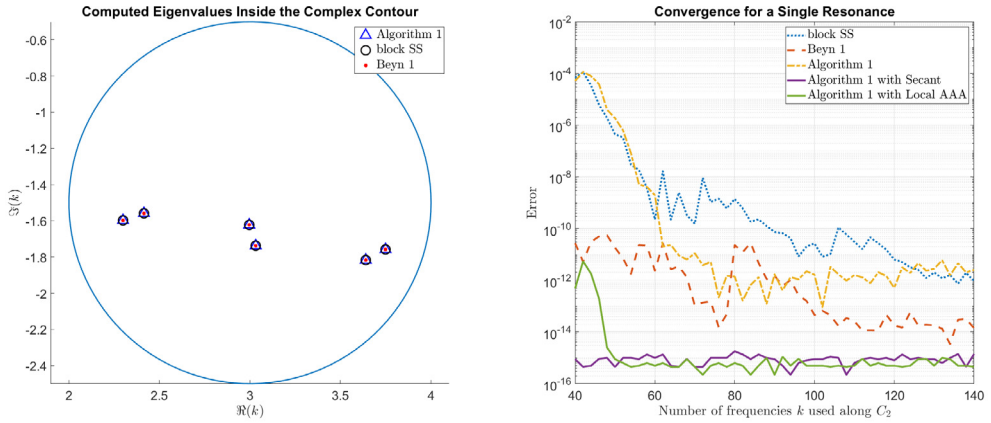

FIG. 4. *Comparison of Algorithm* 1 *to the block SS and Beyn* 1 *methods on the problem of evaluation of scattering poles outside the kite. Left panel: Eigenvalues computed by all three methods. Right panel: Errors computed by comparison with a secant method evaluation of the eigenvalue near* $2.299 - 1.597\mathrm{i}$. *The curves labeled "with secant" were obtained by following the initial eigenvalue determination by four iterations of the secant method. For the curve labeled "with local AAA," four points were sampled on a circle of radius* $1\mathrm{e}-5$ *around the initial AAA approximation of the pole together with a degree* 1 *rational approximant. To avoid underflow the maximum between the error and machine precision is plotted in all cases. The eigenvalues plotted in the left panel are listed in Table* 2.

TABLE 2

Eigenvalues displayed in the left panel of Figure 4. *All digits reported in this table are believed to be correct on the basis of a numerical convergence analysis.*

Exterior kite eigenvalues
$2.299005732126 - 1.597683594805\mathrm{i}$
$2.414612482420 - 1.558932040598\mathrm{i}$
$2.996004574412 - 1.622619819282\mathrm{i}$
$3.031674903510 - 1.737406476233\mathrm{i}$
$3.639478714770 - 1.816722768321\mathrm{i}$
$3.748698135652 - 1.758238284058\mathrm{i}$

a total of L matrix solves per frequency k along the contour, with values of L of the order of, say, a few tens, may prove prohibitively expensive if iterative solutions of large scattering equation systems are involved.

The fact that Algorithm 1 does not utilize a quadrature rule gives rise to a number of additional advantages, briefly mentioned in section 1, vis-à-vis the contour integration–based methods. In particular, the use of rational approximation results in geometric flexibility, such as, e.g., enabling the use of complex frequencies k that lie on a rectangular boundary in the complex plane, or even simple segments along the real axis, which in turn allows for simple adaptive algorithms such as the one introduced in section 5 (Algorithm 2) without suffering a deterioration in convergence. The use of such rectangular domains and associated adaptive algorithms could be envisioned in the context of contour integration–based methods, but may prove suboptimal. Indeed, if the trapezoidal rule is used over a rectangular contour, where the contour integrand is not smooth, a somewhat erratic convergence could result, as illustrated in [25, Fig. 5.1(b)]. If Gauss–Lobatto quadrature is used on each side of a rectangle, in turn, the exponent that characterizes the exponential convergence rate

is the approximately half of the one associated with the trapezoidal rule on a circular contour [25, sect. 5.2]. As a significant additional advantage, Algorithm 2 allows for the reuse of previously used data points as the frequency mesh is refined with the goal of obtaining added accuracy—a strategy which cannot be used in the context of the Gauss–Lobatto quadrature. Finally, the applicability of the proposed algorithms on real segments instead of closed complex contours provides an important benefit, e.g., for applications concerning real eigenvalues.

6.5. Dependence on gap size. With a tool in hand to compute scattering poles quickly and accurately, certain mathematical aspects of their behavior may be considered, such as, e.g., the convergence rate of a complex scattering pole associated with an open arc equal to the difference between a closed curve and a gap section, as the gap size shrinks to zero. As an example we consider the second and third modes shown in the top row of Figure 3, and associated eigenvalues (but for varying gap sizes θ), which for small θ are approximately equal to the lowest double eigenvalue the closed unit circle ($\theta = 0$)—namely the first root ≈ 3.8317 of the Bessel function $J_1(x)$. Figure 5 demonstrates the convergence of $\Re(k)$ (the "spatial frequency") and $\Im(k)$ (the "decay rate") to their limiting values as θ shrinks to zero. The combined set of convergence computations for the two modes considered was completed in approximately four seconds on a single core of a present-day laptop computer.

The first image in Figure 5 shows that for the second mode in Figure 3, whose convergence rate we presume to correspond to generic gap-shrinking eigenvalue convergence behavior, the frequency converges to its limiting value ≈ 3.8317 at the rate $O(\theta^2)$ and the decay rate to its limiting value 0 at the rate $O(\theta^4)$. For the third

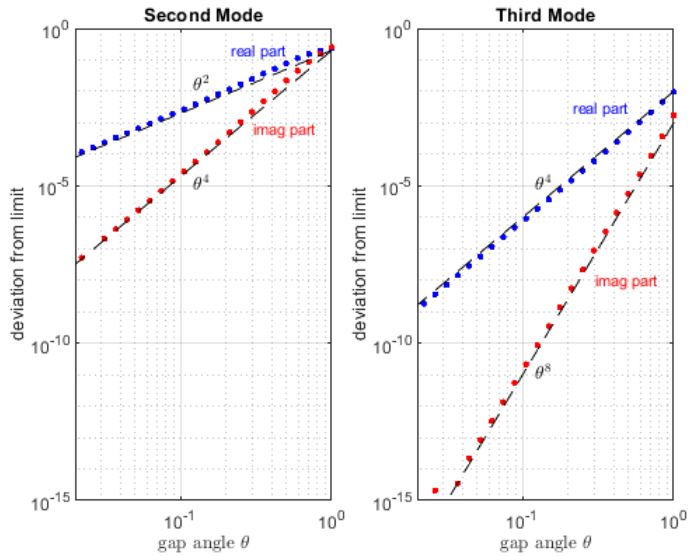

FIG. 5. *Convergence of $\Re(k)$ and $\Im(k)$ to their limiting values as the gap size θ shrinks to zero for the nearly degenerate open circle eigenfunctions displayed as the second and third images on the top row of Figure 3. For both modes the imaginary parts (decay rates) converge at twice the rates of the real parts (spatial frequencies), and both the rates for the real and imaginary parts for the third mode are twice those for the second mode. Note that for the third mode the approximate nodal line is aligned with the gap and thus results in a weaker coupling of interior and exterior fields and associated faster convergence.*

mode in the figure, in turn, the rates double to $O(\theta^4)$ and $O(\theta^8)$. This is related to the alignment of the nodal line of the eigenfunction with the gap, which reduces the field coupling between the interior and exterior regions of the open cavity. We are not aware of any theoretical or computational studies reporting on such convergence rates for scattering poles as opening gaps tend to zero.

The computations of Figures 3 and 5 correspond to Dirichlet boundary conditions, and it is interesting to ask the same questions in the Neumann case. Here the first degenerate eigenvalue for the circle, associated with the first zero of the derivative of $J_1(r)$, is $1.84118\ldots$. Once again, introducing a gap in the boundary breaks the degeneracy. In separate computations (not shown) we have found that for the mode whose nodal line is aligned with the gap, the eigenvalue now converges at the rates θ^2 for the real part and θ^4 for the imaginary part, whereas for the more generic mode whose nodal line is orthogonal to the gap, the rates slow down dramatically to $1/|\log\theta|$ and $1/|\log\theta|^2$, respectively.

6.6. High-frequency examples. Several higher-frequency examples are considered in what follows. To verify the accuracy of the proposed methods in high-frequency cases and in regions containing large numbers of eigenvalues we applied the real line version of Algorithm 2 to obtain all 1244 distinct interior Laplace eigenvalues of the unit circle that are contained in the interval $[1, 100]$. The algorithm automatically obtained all 1244 eigenvalues with near machine accuracy in an average computational time of 1.09 seconds per eigenvalue in a single CPU core. This relatively high computing-time figure is dominated by the higher eigenvalues; for example, the average time per eigenvalue in the interval $[0, 25]$ is only about 0.08 seconds.

Having verified our algorithm in the high-frequency regime, we subsequently applied the proposed methods to several high-frequency eigenvalue problems for interior and open-cavity domains. Figure 6 displays high-frequency interior eigenfunctions for kite-shaped and rocket-shaped cavities. The right panels in Figures 7 and 8, in turn, present eigenfunctions for circular and rocket-shaped open cavities, while the left panels of these figures present the solutions of problems of scattering by the same cavities under vertical upward-facing plane-wave illumination at frequencies equal to the real parts of the eigenvalues associated with the corresponding right panels. Clearly, the left panel scattering solutions bear a close resemblance to the eigenfuncions displayed

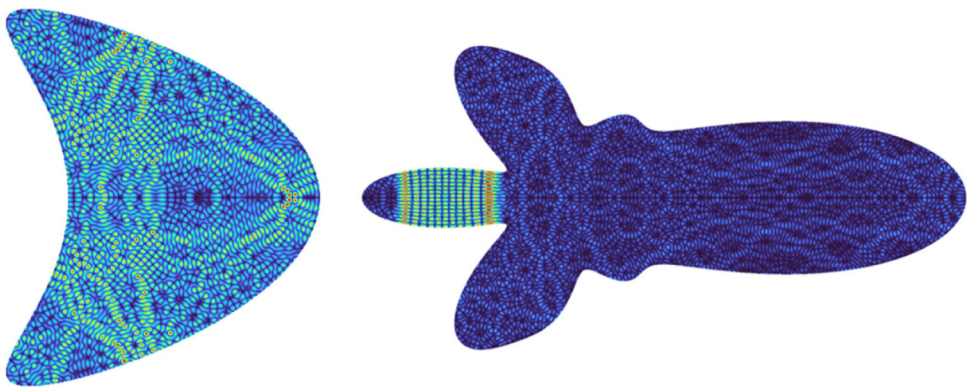

FIG. 6. *Left: Interior eigenfunction for the kite-shaped domain with eigenvalue* 100.1846738596. *Right: Interior eigenfunction for the rocket-shaped domain with eigenvalue* 399.9730212127. *All digits listed are believed correct on the basis of numerical convergence analyses.*

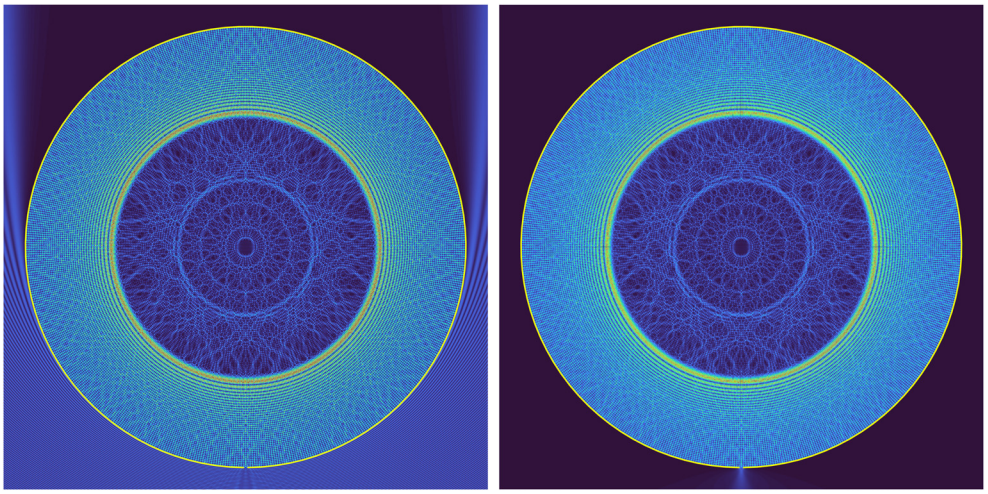

FIG. 7. *Comparison of the solution of the scattering problem with* $k = 499.9073989141$ *under vertical and upward plane-wave incidence (left) and the eigenfunction corresponding to the eigenvalue* $499.9073989141 - 0.000779974959\mathrm{i}$ *(right) for an open circular cavity with aperture size* $\pi/100$. *All digits listed are believed correct on the basis of numerical convergence analyses.*

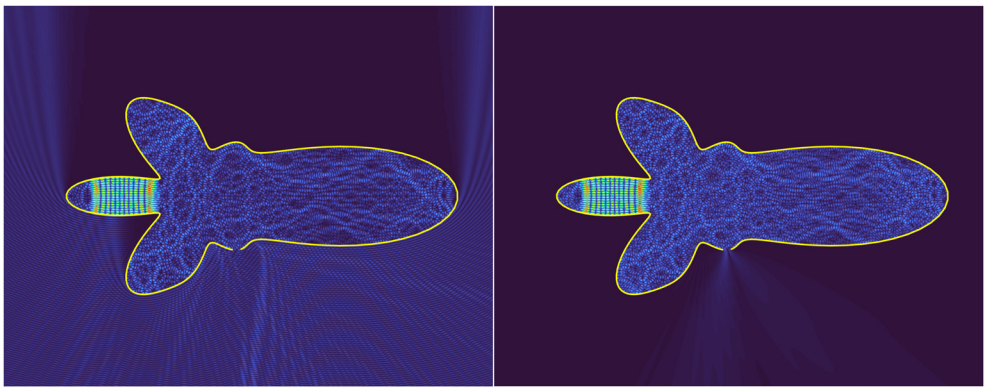

FIG. 8. *Comparison of the solution of the scattering problem with* $k = 399.9694808817$ *under vertical plane-wave incidence (left) and the eigenfunction corresponding to the eigenvalue* $399.9694808817 - 0.00434495360\mathrm{i}$ *(right) for a rocket-like open cavity. The opening in the right curve is approximately equal to* 0.6% *of the curve length. All digits listed are believed correct on the basis of convergence analyses.*

in the right panels, suggesting that the open-cavity eigenfunctions can be excited by adequately oriented incident fields penetrating through the small apertures. All digits displayed in the figure captions have been found to be correct by means of studies of convergence in both the discretization of the integral equations used and of the eigensearch algorithms utilized. For reference in Figures 7 and 8, the most refined solution used 16 points per wavelength, which led to matrix discretizations of size 5000×5000 and 4000×4000, respectively, and produced 13-digit accuracies.

7. Conclusions. This paper introduced a novel numerical algorithm for the evaluation of real and complex eigenvalues and eigenfunctions of general NEPs, including NEPs associated with Laplace eigenvalue and scattering resonance problems

for open and closed domains. Based on use of adaptive eigenvalue search methods based on AAA rational approximation combined with secant method refinement, the algorithm produces highly accurate eigenpairs for challenging eigenproblems at both low and high frequencies. Comparisons with well-known contour integration methods demonstrated a number of advantages of the proposed approach, including fast convergence and geometric flexibility. The latter characteristic is significant, in that it greatly facilitates use of the algorithm in a rectangular refinement-based adaptive strategy—resulting in automatic evaluation of all eigenvalues contained within a given region with near machine precision accuracy.

Appendix A. Almost-sure pole detection via the randomly scalarized resolvent $S(k)$. This appendix establishes that for probability distributions that are absolutely continuous with respect to the Lebesgue measure, the poles of the randomly scalarized resolvent $S(k)$ coincide, with probability 1, with the poles of the resolvent F_k^{-1}. The proof relies in part on the following simple lemma.

LEMMA 1. *Let $A_m \in \mathbb{C}^{d\times d}$, $m \in \mathbb{N}$, denote a sequence of $d \times d$ matrices such that $\|A_m\|_{\mathrm{e},\infty} \to \infty$ as $m \to \infty$, where, for a matrix $B \in \mathbb{C}^{d\times d}$,*

$$\|B\|_{\mathrm{e},\infty} = \max_{1\le i,j\le d} |(B)_{ij}| \tag{17}$$

denotes the entrywise matrix infinity norm. Then there exists a subsequence A_{m_p}, an index pair (i_0, j_0), $1 \le i_0, j_0 \le d$, and a matrix $A \in \mathbb{C}^{d\times d}$ such that

$$\lim_{p\to\infty} |(A_{m_p})_{i_0 j_0}| = +\infty, \quad \lim_{p\to\infty} A_{m_p}/|(A_{m_p})_{i_0 j_0}| = A, \quad \text{and} \quad A \neq 0. \tag{18}$$

Proof. For all $m \ge 1$, the matrix $A_m/\|A_m\|_{\mathrm{e},\infty}$ is contained within the unit ball in $\mathbb{C}^{d\times d}$ in the entrywise matrix infinity norm (17). Since the finite-dimensional unit ball is a compact set, we may select a sequence m_p of integers such that $A_{m_p}/\|A_{m_p}\|_{\mathrm{e},\infty}$ converges as $p \to \infty$: $\lim_{p\to\infty} A_{m_p}/\|A_{m_p}\|_{\mathrm{e},\infty} = A$ for some matrix $A \in \mathbb{C}^{d\times d}$. By passing to a further subsequence if necessary, we may assume that there exists a fixed pair $(i_0, j_0) \in \mathbb{N}^2$ such that

$$|(A_{m_p})_{i_0 j_0}| = \|A_{m_p}\|_{\mathrm{e},\infty} \quad \text{for all } p \in \mathbb{N} \quad \text{and, thus,} \quad \lim_{p\to\infty} A_{m_p}/|(A_{m_p})_{i_0 j_0}| = A.$$

It follows in particular that $\lim_{p\to\infty} |(A_{m_p})_{i_0 j_0}| = +\infty$. Since $|\frac{(A_{m_p})_{i_0 j_0}}{\|A_{m_p}\|_{\mathrm{e},\infty}}| = 1$ for all $p \in \mathbb{N}$, further, the limit matrix A satisfies $|A_{i_0 j_0}| = 1 \neq 0$, so that $A \neq 0$, and the proof is complete. ∎

THEOREM 2. *Let $u, v \in \mathbb{C}^d$ be random vectors drawn from a probability measure P such that $P \times P$ is absolutely continuous with respect to the Lebesgue measure in $\mathbb{C}^{2d}$. Then, with $P \times P$ probability 1, the poles of $S(k; u, v)$ in (4) coincide with the poles of the resolvent F_k^{-1} in the variable k.*

Proof. The complex number k_0 is a pole of the resolvent F_k^{-1} if and only if there exists a vector $w^0 \in \mathbb{C}^d$ such that

$$F_k^{-1} w^0 \to \infty \quad \text{as} \quad k \to k_0. \tag{19}$$

Thus, selecting, for each such pole k_0, a sequence $k_m \to k_0$ such that F_{k_m} is invertible for all m, (19) tells us that the m-dependent matrix $A_m = F_{k_m}^{-1}$ tends to infinity as $m \to \infty$ in the entrywise infinity norm (17). In view of Lemma 1 it follows that the

statement (18) holds for some sequence m_p, some index pair (i_0, j_0) with $1 \le i_0, j_0 \le d$, and some matrix A.

Let now $u, v \in \mathbb{C}^d$ be given vectors. If $k = k_0$ is not a pole of $S(k; u, v)$, then

$$S(k_{m_p}; u, v) = u^* A_{m_p} v = |(A_{m_p})_{i_0 j_0}| \frac{u^* A_{m_p} v}{|(A_{m_p})_{i_0 j_0}|}$$

is bounded for p large enough, and since, in view of (18), $|(A_{m_p})_{i_0 j_0}| \to \infty$ as $p \to \infty$, it follows that

$$0 = \lim_{p \to \infty} \frac{u^* A_{m_p} v}{|(A_{m_p})_{i_0 j_0}|} = u^* A v. \tag{20}$$

It is easy to check that, since $A \neq 0$, the set of pairs $(u, v) \in \mathbb{C}^d \times \mathbb{C}^d = \mathbb{C}^{2d}$ satisfying (20) has zero Lebesgue measure (cf., e.g., [23, Cor. 10, sect. I(A)]). Consequently, this set also has probability zero with respect to the product measure $P \times P$, which completes the proof. ∎

Appendix B. Laplace eigenvalue determination for open arc problems via integral equations. This section provides a proof of the open-arc components of Theorem 1 by generalizing the closed-curve analysis in [41, sect. 9.7]. To prepare for the proof we define the Sobolev space $H_e^s(2\pi)$ of 2π even functions [12, Def. 2.3] that underlies the definition of the open arc integral operator (9).

DEFINITION 1. *For $s \in \mathbb{R}$, the Sobolev space $H_e^s(2\pi)$ is defined as the completion of the space of infinitely differentiable 2π-periodic and even functions defined in the real line with respect to the norm*

$$\|v\|^2_{H_e^s(2\pi)} = |a_0| + 2 \sum_{m=1}^{\infty} m^{2s} |a_m|^2,$$

where a_m denotes the mth cosine coefficient of v:

$$v(\theta) = \frac{1}{2} a_0 + \sum_{m=1}^{\infty} a_m \cos(m\theta). \tag{21}$$

The proofs of the open-arc portions of Theorem 1 additionally rely on the solution operator $\mathcal{U}_k^o : H_e^s(2\pi) \to H^1_{\mathrm{loc}}(\Omega)$ for the open-arc Helmholtz problem which, for given boundary data $B \in H_e^s(2\pi)$, returns the solution $u = \mathcal{U}_k^o[B]$ of (1) satisfying the Dirichlet boundary condition $u|_\Gamma = B$ and the radiation condition

$$\lim_{|x| \to \infty} \sqrt{|x|} \left(\frac{\partial u}{\partial |x|} - iku \right) = 0 \quad \text{uniformly in all directions } x/|x|. \tag{22}$$

As is well known, this operator can be expressed in terms of the single-layer potential $\mathcal{S}_k$ and the boundary integral operator F_k (9) and (11):

$$\mathcal{U}_k^o[B] = \mathcal{S}_k[F_k^{-1}[B]]. \tag{23}$$

The operator F_k is invertible for all k in the set $\mathcal{K} = \{k \mid \Im k \ge 0 \text{ and } k \neq 0\}$ [39], and, thus, the solution operator is well defined and analytic for all $k \in \mathcal{K}$. Additionally, as shown in the following lemma, the solution operator $\mathcal{U}_k^o$ extends meromorphically into $\mathbb{C} \setminus \gamma$ for any logarithmic branch-cut curve γ.

LEMMA 2. *Let γ denote an arbitrary continuous curve connecting 0 and ∞ in the complex plane. Then, the inverse operator F_k^{-1} and the solution operator $\mathcal{U}_k^{\mathrm{o}}$ extend meromorphically to $\mathbb{C}\setminus\gamma$, with poles located in the lower half-plane set $\{\Im k<0\}$.*

Proof. Using the (invertible) flat-arc zero-frequency operator [12, 29]

(24)
$$F_0^\tau[\widetilde{\psi}](\theta) = -\frac{1}{2\pi}\int_0^\pi \ln|\cos(\theta)-\cos(\theta')|\widetilde{\psi}(\theta')\tau(\cos(\theta'))d\theta', \quad F_0 : H_e^s(2\pi)\to H_e^{s+1}(2\pi),$$

and defining the operator

$$C_k = (F_0^\tau)^{-1}(F_k - F_0^\tau), \quad C_k : H_e^s(2\pi)\to H_e^{s+1}(2\pi), \tag{25}$$

which is compact operator for all $k\neq 0$, the frequency-k operator F_k (9) may be expressed in the form [29, eq. 4.17]

$$F_k = F_0^\tau(I+C_k).$$

Since F_k is invertible for all $k\in\mathcal{K}$, the lemma follows from the well-known fact that the resolvent of a Fredholm operator is meromorphic (see, e.g., [41, Chap. 9, Prop. 7.4]). ∎

In view of Lemma 2, (23) implies that the set of poles of $\mathcal{U}_k^{\mathrm{o}}$ is a subset of the set of poles of F_k^{-1}. But, in fact, these two sets coincide.

LEMMA 3. *A value $k=k_0$ is a pole of the solution operator $\mathcal{U}_k^{\mathrm{o}}$ if and only if it is a pole of the resolvent F_k^{-1}.*

Proof. We begin by noting that the single-layer potential $\mathcal{S}_k$ is injective. This follows from the continuity of $\mathcal{S}_k[\widetilde{\psi}]$ for $x\in\Gamma$, along with the jump relations for its normal derivative across Γ [17, 31]. These properties together imply that if $\mathcal{S}_k[\widetilde{\psi}]$ vanishes identically in Ω, then $\widetilde{\psi}=0$.

To proceed with the proof, assume that the resolvent operator F_k^{-1} has a pole of order m at $k=k_0$. Then there exists a function $B\in H_e^{s+1}(2\pi)$ such that

$$F_k^{-1}[B] = (k-k_0)^{-m}\left(B_m + B_{m+1}(k-k_0)+\cdots\right), \tag{26}$$

for some sequence of functions $B_j\in H_e^s(2\pi)$ with $j\geq m$, where $B_m\neq 0$. Letting $u_m=\mathcal{S}_k[B_m]$ it follows that

$$\mathcal{U}_k^{\mathrm{o}}[B] = (k-k_0)^{-m}u_m + O((k-k_0)^{-m+1}) \quad \text{as} \quad k\to k_0.$$

By the injectivity of $\mathcal{S}_k$ we know $u_m\neq 0$, and therefore k_0 is a pole of $\mathcal{U}_{\mathrm{o}}$. ∎

We are now ready to prove the open-arc portions of Theorem 1.

Proof of Theorem 1 (open arc). We begin by establishing the equivalence of points (i) and (ii). Suppose (i) holds for some $k_0\in\mathbb{C}$. Then F_k is not invertible at k_0, and by Lemma 2, it follows that (ii) must hold. Conversely, suppose k_0 is a pole of F_k^{-1}. As in the proof of Lemma 3, there exists a function $B\in H_e^{s+1}(2\pi)$ such that the expansion (26) holds. Applying F_k to both sides of (26), we obtain

$$B = (k-k_0)^{-m}\left(F_k[B_m] + F_k[B_{m+1}](k-k_0)+\cdots\right).$$

Taking the limit as $k\to k_0$ implies that $F_k[B_m]\to 0$. Since $B_m\neq 0$, this shows that (ii) implies (i). Point (iii) was established in Lemma 2. To prove point (iv), assume that

k_0^2 is an eigenvalue of the boundary value problem (1)–(2). Then the solution operator $\mathcal{U}_k^{\circ}$ must have a pole at either k_0 or $-k_0$, whichever lies in the lower half-plane. By Lemma 3, this implies that F_k^{-1} also has a pole at that point.

Conversely, suppose that k_0 is a pole of F_k^{-1}. Then, by the equivalence of points (i) and (ii), there exists a nonzero function $\widetilde{\psi}$ such that $F_{k_0}[\widetilde{\psi}] = 0$. Defining $u = \mathcal{S}_{k_0}[\widetilde{\psi}]$, it follows that the pair (u, k_0^2) satisfies the eigenvalue problem (1)–(2) with radiation condition (6). This completes the proofs of points (iv) and (v) and thus concludes the proof of the open arc portion of Theorem 1. ∎

Acknowledgments. The authors acknowledge valuable feedback from the reviewers and helpful discussions with the following individuals: Stefan Güttel, Jonathan Keating, Yuji Nakatsukasa, Ory Schnitzer, Euan Spence, and Maciej Zworski.

REFERENCES

[1] G. Acosta, J. P. Borthagaray, O. Bruno, and M. Maas, *Regularity theory and high order numerical methods for the (1D)-fractional Laplacian*, Math. Comput., 87 (2018), pp. 1821–1857, https://doi.org/10.1090/mcom/3276.

[2] E. Akhmetgaliyev and O. P. Bruno, *Regularized integral formulation of mixed Dirichlet-Neumann problems*, J. Integral Equations Appl., 29 (2017), pp. 493–529, https://doi.org/10.1216/JIE-2017-29-4-493.

[3] E. Akhmetgaliyev, O. P. Bruno, and N. Nigam, *A boundary integral algorithm for the Laplace Dirichlet–Neumann mixed eigenvalue problem*, J. Comput. Phys., 298 (2015), pp. 1–28, https://doi.org/10.1016/j.jcp.2015.05.016.

[4] C. J. Alves and P. R. Antunes, *Wave scattering problems in exterior domains with the method of fundamental solutions*, Numer. Math., 156 (2024), pp. 1–20, https://doi.org/10.1007/s00211-024-01395-x.

[5] J. Asakura, T. Sakurai, H. Tadano, T. Ikegami, and K. Kimura, *A numerical method for nonlinear eigenvalue problems using contour integrals*, JSIAM Lett., 1 (2009), pp. 52–55, https://doi.org/10.14495/jsiaml.1.52.

[6] C. E. Baum, *The singularity expansion method*, in Transient Electromagnetic Fields, L. B. Felsen, ed., Springer, Berlin, 1976, pp. 129–179, https://doi.org/10.1007/3540075534_8.

[7] T. Betcke, N. J. Higham, V. Mehrmann, C. Schröder, and F. Tisseur, *NLEVP: A collection of nonlinear eigenvalue problems*, ACM Trans. Math. Software, 39 (2013), pp. 1–28, https://doi.org/10.1145/2427023.2427024.

[8] F. Betz, M. Hammerschmidt, L. Zschiedrich, S. Burger, and F. Binkowski, *Efficient rational approximation of optical response functions with the AAA algorithm*, Laser Photonics Rev., 18 (2024), https://doi.org/10.1002/lpor.202400584.

[9] W.-J. Beyn, *An integral method for solving nonlinear eigenvalue problems*, Linear Algebra Appl., 436 (2012), pp. 3839–3863, https://doi.org/10.1016/j.laa.2011.03.030.

[10] F. Binkowski, F. Betz, M. Hammerschmidt, L. Zschiedrich, and S. Burger, *Resonance modes in microstructured photonic waveguides: Efficient and accurate computation based on AAA rational approximation*, Nanophotonics, 14 (2025), pp. 1665–1671, https://doi.org/10.1515/nanoph-2024-0755.

[11] O. P. Bruno, V. Domínguez, and F.-J. Sayas, *Convergence analysis of a high-order Nyström integral-equation method for surface scattering problems*, Numer. Math., 124 (2013), pp. 603–645, https://doi.org/10.1007/s00211-013-0525-9.

[12] O. P. Bruno and S. K. Lintner, *Second-kind integral solvers for TE and TM problems of diffraction by open arcs*, Radio Sci., 47 (2012), pp. 1–13, https://doi.org/10.1029/2012RS005035.

[13] O. P. Bruno and S. K. Lintner, *A high-order integral solver for scalar problems of diffraction by screens and apertures in three-dimensional space*, J. Comput. Phys., 252 (2013), pp. 250–274, https://doi.org/10.1016/j.jcp.2013.06.022.

[14] D. A. Bykov and L. L. Doskolovich, *Numerical methods for calculating poles of the scattering matrix with applications in grating theory*, J. Lightwave Technol., 31 (2012), pp. 793–801, https://doi.org/10.1109/JLT.2012.2234723.

[15] Y. Chahlaoui and P. Van Dooren, *A Collection of Benchmark Examples for Model Reduction of Linear Time Invariant Dynamical Systems*, E-Print 2008.22, Manchester Institute for Mathematical Sciences, University of Manchester, Manchester, UK, 2002.

[16] M. J. Colbrook and A. Townsend, *Avoiding discretization issues for nonlinear eigenvalue problems*, SIAM J. Matrix Anal. Appl., 46 (2025), pp. 648–675, https://doi.org/10.1137/23M1569927.
[17] D. L. Colton and R. Kress, *Integral Equation Methods in Scattering Theory*, John Wiley & Sons, New York, 1983.
[18] D. L. Colton and R. Kress, *Inverse Acoustic and Electromagnetic Scattering Theory*, 4th ed., Springer, Cham, 2019.
[19] M. Costabel, M. Dauge, and R. Duduchava, *Asymptotics without logarithmic terms for crack problems*, Comm. Partial Differential Equations, 28 (2003), pp. 869–926, https://doi.org/10.1081/PDE-120021180.
[20] T. A. Driscoll, N. Hale, and L. N. Trefethen, *Chebfun Guide*, 2014, www.chebfun.org.
[21] M. El-Guide, A. Międlar, and Y. Saad, *A rational approximation method for solving acoustic nonlinear eigenvalue problems*, Eng. Anal. Bound. Elem., 111 (2020), pp. 44–54, https://doi.org/10.1016/j.enganabound.2019.10.006.
[22] S. Elsworth and S. Güttel, *Conversions between barycentric, RKFUN, and Newton representations of rational interpolants*, Linear Algebra Appl., 576 (2019), pp. 246–257, https://doi.org/10.1016/j.laa.2018.10.003.
[23] R. C. Gunning and H. Rossi, *Analytic Functions of Several Complex Variables*, AMS Chelsea Publ. 368, AMS, Providence, RI, 1965.
[24] S. Güttel, G. M. Negri Porzio, and F. Tisseur, *Robust rational approximations of nonlinear eigenvalue problems*, SIAM J. Sci. Comput., 44 (2022), pp. A2439–A2463, https://doi.org/10.1137/20M1380533.
[25] S. Güttel and F. Tisseur, *The nonlinear eigenvalue problem*, Acta Numer., 26 (2017), pp. 1–94, https://doi.org/10.1017/S0962492917000034.
[26] F. Klopp and M. Zworski, *Generic simplicity of resonances*, Helv. Phys. Acta, 68 (1995), pp. 531–538.
[27] A. Leblanc and A. Lavie, *Solving acoustic nonlinear eigenvalue problems with a contour integral method*, Eng. Anal. Bound. Elem., 37 (2013), pp. 162–166, https://doi.org/10.1016/j.enganabound.2012.09.007.
[28] P. Lietaert, K. Meerbergen, J. Pérez, and B. Vandereycken, *Automatic rational approximation and linearization of nonlinear eigenvalue problems*, IMA J. Numer. Anal., 42 (2022), pp. 1087–1115, https://doi.org/10.1093/imanum/draa098.
[29] S. K. Lintner and O. P. Bruno, *A generalized Calderón formula for open-arc diffraction problems: Theoretical considerations*, Proc. Roy. Soc. Edinburgh, 145 (2015), pp. 331–364, https://doi.org/10.1017/S0308210512000807.
[30] Y. Ma and J. Sun, *Computation of scattering poles using boundary integrals*, Appl. Math. Lett., 146 (2023), 108792, https://doi.org/10.1016/j.aml.2023.108792.
[31] W. C. H. McLean, *Strongly Elliptic Systems and Boundary Integral Equations*, Cambridge University Press, Cambridge, UK, 2000.
[32] V. Mehrmann and D. Watkins, *Polynomial eigenvalue problems with Hamiltonian structure*, Electron. Trans. Numer. Anal., 13 (2002), pp. 106–118.
[33] R. Misawa, K. Niino, and N. Nishimura, *Boundary integral equations for calculating complex eigenvalues of transmission problems*, SIAM J. Appl. Math., 77 (2017), pp. 770–788, https://doi.org/10.1137/16M1087436.
[34] Y. Nakatsukasa, O. Sète, and L. N. Trefethen, *The AAA algorithm for rational approximation*, SIAM J. Sci. Comput., 40 (2018), pp. A1494–A1522, https://doi.org/10.1137/16M1106122.
[35] H. W. Pommerenke, J. D. Heller, S. G. Zadeh, and U. van Rienen, *Computation of lossy higher order modes in complex SRF cavities using Beyn's and Newton's methods on reduced order models*, Internat. J. Modern Phys. A, 34 (2019), 1942037, https://doi.org/10.1142/S0217751X19420375.
[36] L. Reichel and Q. Ye, *Breakdown-free GMRES for singular systems*, SIAM J. Matrix Anal. Appl., 26 (2005), pp. 1001–1021, https://doi.org/10.1137/S0895479803437803.
[37] C. Sideris, D. Aslanyan, and O. P. Bruno, *High order-accurate solution of scattering integral equations with unbounded solutions at corners*, J. Comput. Phys., 539 (2025), 114213, https://doi.org/10.1016/j.jcp.2025.114213.
[38] O. Steinbach and G. Unger, *Convergence analysis of a Galerkin boundary element method for the Dirichlet Laplacian eigenvalue problem*, SIAM J. Numer. Anal., 50 (2012), pp. 710–728, https://doi.org/10.1137/100801986.
[39] E. P. Stephan and W. L. Wendland, *An augmented Galerkin procedure for the boundary integral method applied to two-dimensional screen and crack problems*, Appl. Anal., 18 (1984), pp. 183–219, https://doi.org/10.1080/00036818408839520.

[40] J. Stoer and R. Bulirsch, *Introduction to Numerical Analysis*, Texts Appl. Math. 1993, Springer, Berlin, 1980.
[41] M. E. Taylor, *Partial Differential Equations*. II, Springer-Verlag, New York, 1996.
[42] C. Wieners and J. Xin, *Boundary element approximation for Maxwell's eigenvalue problem*, Math. Methods Appl. Sci., 36 (2013), pp. 2524–2539, https://doi.org/10.1002/mma.2772.
[43] L. Zhao and A. Barnett, *Robust and efficient solution of the drum problem via Nyström approximation of the Fredholm determinant*, SIAM J. Numer. Anal., 53 (2015), pp. 1984–2007, https://doi.org/10.1137/140973992.
[44] F. Zolla, G. Renversez, A. Nicolet, B. Kuhlmey, S. R. Guenneau, and D. Felbacq, *Foundations of Photonic Crystal Fibres*, World Scientific, River Edge, NJ, 2005.